Available online at www.sciencedirect.com

ScienceDirect

Advances in Space Research xxx (xxxx) xxx

ADVANCES IN SPACE RESEARCH (a COSPAR publication)

www.elsevier.com/locate/asr

URE and URA for predicted LEO satellite orbits at different altitudes

Kan Wang [a,b,*], Ahmed El-Mowafy [c], Xuhai Yang [a,b]

[a] National Time Service Center, Chinese Academy of Sciences, Xi'an 710600, China
[b] University of Chinese Academy of Sciences, Beijing 100049, China
[c] School of Earth and Planetary Sciences, Curtin University, Perth, WA 6845, Australia

Received 6 May 2022; received in revised form 12 August 2022; accepted 14 August 2022

Abstract

In recent years, low Earth orbit (LEO) satellites have been frequently discussed for their benefits in positioning and navigation services as an augmentation to the global navigation satellite systems (GNSSs). Similar to the positioning concept based on ranging to GNSS satellites, precise positioning of single-receiver users needs high-accuracy orbits and clocks of LEO satellites as a pre-condition. For real-time users, high prediction accuracies of these orbits at different latencies are needed. Unlike the satellite clocks, the GNSS orbits can be typically predicted for hours with high accuracy. LEO satellites, however, face more complicated perturbing dynamic terms due to their low altitudes. Therefore, the prediction accuracy and integrity of their orbits need to be addressed. In this study, using real data of three test LEO satellites GRACE C, Sentinel-1A and Sentinel-3B of different altitudes, various reduced-dynamic prediction strategies are assessed, with the appropriate methods selected for different prediction times up to 6 h. The global-averaged orbital user range errors (OUREs) are shown to be altitude-related. For the 700–800 km Sentinel satellites and 500 km GRACE satellite, the RMS of the OUREs is at sub-dm and dm-level for the prediction time of 1 h, respectively, and around 0.2 m and 0.6 m at the prediction time of 6 h, respectively. For integrity purposes, the worst-location OURE are calculated for the predicted orbits using a proposed algorithm considering the Earth as an Ellipsoid, not a sphere as usually done for the GNSS satellites. The orbital user range accuracy (OURA) is then evaluated for different prediction periods, having a time-dependent model proposed to compute the overbounding OURA at any prediction time within 6 h. With an integrity risk of 10^{-5}, using hourly quadratic polynomials as the time-dependent model, the overbounding OURA is around 0.1 m at the prediction of 1 h, and at the sub-meter level for the prediction of 6 h for the Sentinel satellites.

Keywords: Low Earth orbit (LEO); Orbit prediction; URE; URA; GNSS

1. Introduction

Recently, the use of low Earth orbit (LEO) satellites is frequently discussed to serve as an augmentation to the traditional global navigation satellite systems (GNSSs) in the positioning and navigation services. Due to their much lower orbital heights, LEO satellites have numerous advantages compared to GNSS satellites, such as they have much stronger signal strength, nearly whitened multipath effects, and fast geometry change (Reid et al. 2018). When augmenting GNSS observations, the convergence time of the widely used precise point positioning (PPP) approach can be shortened from tens of minutes to only a few minutes (or even less) (Ge et al. 2018; Li et al. 2018a). LEO satellites are involved in future navigation satellite systems such as the Kepler system designed by the German Aerospace Center (DLR) (Michalak et al. 2021) and the Chinese CentiSpace system (Yang 2019; Wang et al. 2022).

To realize the various benefits brought by the LEO satellites, e.g., in PPP, high-precision orbital products are

* Corresponding author at: National Time Service Center, Chinese Academy of Sciences, Xi'an 710600, China.
E-mail address: wangkan@ntsc.ac.cn (K. Wang).

https://doi.org/10.1016/j.asr.2022.08.039
0273-1177/

required. Nowadays, LEO precise orbit determination (POD) can typically reach an accuracy of centimeters in the reduced-dynamic mode (Gu et al. 2017; Li et al. 2018b), with GNSS receivers on board, by using undifferenced GNSS observations and post-processed high-precision GNSS orbital and clock products. Higher POD accuracy, within 1 cm, was also reported by Mao et al. (2021) by resolving single-receiver ambiguities and reducing the stochastic empirical parameters with refined dynamic models. In 'near' real-time, the orbital accuracy of LEO satellites is degraded mainly due to the decreased accuracy of real-time GNSS products. Even when using high-precision GNSS products on the ground or from geostationary (GEO) satellites, the 3-dimensional (3D) root-mean-square error (RMSE) is generally at the sub-dm to dm-level (Wermuth et al. 2012; Hauschild et al. 2016; Allahvirdi-Zadeh et al. 2021), depending on the processing mode and the products used.

On the ground, high-precision real-time positioning users face latencies for the LEO orbital and clock products of different terms. Assuming the onboard GNSS observations can be transmitted to Earth, the latency of the orbital products of LEO satellites that could vary from seconds to hours would depend on several factors. These include the data transmission time, the processing time, the product transmission time and their sampling interval, and the Internet status. The real-time users, in practice, would use predicted LEO satellite orbits. Unlike the GNSS satellites, the LEO satellites are challenging to be continuously observed by the ground network due to their low altitudes and the resulting small footprints on Earth (Cakaj et al. 2014). Depending on the network density and distribution that computes LEO orbital products, the interval between subsequent direct downlinks from the same LEO satellite could last for hours (Wang and El-Mowafy 2020), not to mention possible signal interruptions. With the help of the inter-satellite links, the transmission of at least the onboard observations could be enabled in a much more efficient way (Jia et al. 2017). However, depending on the POD strategy, orbit prediction for a few hours could still be needed. Taking an example from GNSS satellites, the ultra-rapid orbits provided by the International GNSS Service (IGS) has a latency of 3–9 h for the observed part (Springer and Hugentobler 2001; Johnston et al. 2017), which implies the same prediction interval. For the IGS real-time service (RTS) (Hadas and Bosy 2015), analysis centers also often estimate high-sampling satellite clocks using predicted orbits of a few hours (RTS Contributors 2022).

The prediction errors of the LEO satellite orbits are impacted by various factors. Satellites at low altitudes usually face strong and complicated drag effects, which are correlated with the geomagnetic and solar activities, especially in the long term (Arbinger and D'Amico 2004; He et al. 2020). Wang and El-Mowafy (2020) extended the 500 km orbits of the GRACE Follow-on satellite GRACE-C by using constant and periodic dynamic parameters and stochastic accelerations/velocities. The 3D RMSE of the predicted orbits was about 0.17 m at 1 h. Ge et al. (2020) showed that for GRACE-A satellite of about 500 km altitude, the 3D RMSE of the predicted orbits at 1 h prediction time without the accelerometer is at sub-meter level, while employing the accelerometer data has reduced the 3D RMSE to the sub-dm level. For satellites with higher orbits, e.g., HY-2A with an altitude of about 970 km, Wang et al. (2016) obtained a 3D RMSE of a few decimeters at 12 h prediction time by using an appropriate fitting interval and employing the empirical CODE orbit model (ECOM) for solar radiation pressure. It can be observed that the LEO orbital prediction errors, on the one side are correlated with the prediction strategy used, but on the other side are highly correlated with the orbital altitude and the prediction time. For prediction up to a few hours, different dynamic models and fitting intervals need to be assessed, and accordingly best ones would be selected for satellites at different altitudes. A comprehensive analysis using real LEO satellite orbits at different heights could deliver a general overview of the orbital contribution of the user range error (OURE) for different prediction times, and for satellites at different altitude levels. This involves, at the same time, the prediction models to be applied. The study of LEO orbit prediction as mentioned above is the first focus of this contribution. It is performed based on real data of three LEO satellites of different altitudes, i.e., the GRACE-C, the Sentinel-1A and the Sentinel-3B, which share similar conditions of future LEO satellites that could be used for positioning.

Integrity monitoring is essential for safety of the positioning users. The protection level (PL) is computed to bound the positioning error under a pre-defined integrity risk. The integrity monitoring of the single-receiver ground-based or aeronautical users often requires, in addition to the orbital corrections, the integrity parameters of the satellite orbits. The user range accuracy (URA), with the corresponding index contained in the broadcast ephemeris of the navigation message, is a main parameter that is used for the computation of the PLs. Under the legacy level of integrity assurance of GPS, 4.42 $\times$ URA is expected to bound the worst-location user range errors (UREs) with a probability of ($1\text{-}10^{-5}$) per hour, for which no alert is sent within 8 s (NAVSTAR 2021). As our second focus, this study attempts to construct an aging-time-related model for the estimation of the orbital user range accuracy (OURA) for LEO satellites. Due to the much lower altitudes of LEO compared to the GNSS Medium Earth Orbit (MEO) satellites, an algorithm is proposed to compute the worst-location orbital user range error (OURE) considering the Earth as a realistic ellipsoid instead of a sphere. Based on real data of the three test satellites (the GRACE-C, the Sentinel-1A and the Sentinel-3B), using the prediction strategies selected, the OURA is evaluated for a prediction time up to 6 h.

Piece-wise quadratic polynomials are generated to overbound the predicted OURA within pre-defined intervals, so that users can compute the overbounding OURA at any time within the prediction interval just using a few sets of polynomial coefficients.

The paper starts by introducing the orbit prediction strategies and the procedure to compute the worst-location OURE and the OURA. The LEO orbital prediction errors are then analyzed for satellites at different altitudes, using various strategies and for different prediction periods. Next, the worst-location OUREs are calculated for all the three test satellites, with their real and overbounding OURA analyzed and discussed for different polynomial fitting intervals. The conclusions are given at the end.

2. Processing strategy

This section is split into two parts. In the first part, the strategies to predict LEO satellite orbits used in this study are discussed. The second part focuses on the methods to derive the worst-location OURE, and next, the OURA.

2.1. LEO satellite orbit prediction

As mentioned in the introduction, the LEO satellite orbits can be determined with a relatively good accuracy using kinematic or reduced-dynamic methods, as long as the dual-frequency code and phase GNSS observations collected onboard exhibit good continuity and quality, and the satellite attitudes are well controlled and determined (Wang et al. 2020). This study does not focus on the determination of the LEO satellite orbits, but only their prediction. Having the high-precision LEO satellite orbital estimates over a period of time, a series of dynamic orbital parameters can be fitted over a certain fitting interval. As a complement to the two-body term of the Earth's gravity and the perturbing accelerations based on existing models (see Table 1), these dynamic parameters can be used to compensate for the accelerations that cannot be perfectly modeled, e.g., those caused by the solar radiation pressure and the air drag (Dach et al. 2015; Li et al. 2018b).

The orbital parameters can be fitted with the least-squares adjustment based on the following linearized equations:

$$E\left(\hat{X}_{\mathrm{L}}(t_i)\right) = A_{\mathrm{K}}(t_i)X_{\mathrm{K}}(t_0) + A_{\mathrm{P}}(t_i)X_{\mathrm{P}} + A_{\mathrm{Sto}}(t_i)X_{\mathrm{Sto}} \tag{1}$$

where $\widehat{X}_{\mathrm{L}}(t_i)$ denotes the 3D vector of the LEO satellite orbital estimates in the Earth-centered Earth-fixed (ECEF) system at time t_i within the fitting interval T_{fit}. $\mathrm{E}(\cdot)$ is the expectation operator. $X_{\mathrm{K}}(t_0)$ represents the Keplerian elements at the initial condition. X_{P} contains the 3D constant (R_0, S_0, W_0), sine (R_{S}, S_{S}, W_{S}) and cosine terms (R_{C}, S_{C}, W_{C}) of the once-*per*-revolution accelerations a_{P}:

$$a_{\mathrm{P}} = a_{\mathrm{P,R}}e_{\mathrm{R}} + a_{\mathrm{P,S}}e_{\mathrm{S}} + a_{\mathrm{P,W}}e_{\mathrm{W}} \tag{2}$$

$$a_{\mathrm{P,R}} = R_0 + R_{\mathrm{C}} \times \cos(U) + R_{\mathrm{S}} \times \sin(U) \tag{3}$$

$$a_{\mathrm{P,S}} = S_0 + S_{\mathrm{C}} \times \cos(U) + S_{\mathrm{S}} \times \sin(U) \tag{4}$$

$$a_{\mathrm{P,W}} = W_0 + W_{\mathrm{C}} \times \cos(U) + W_{\mathrm{S}} \times \sin(U) \tag{5}$$

where the subscripts R, S and W denote the radial, along-track and cross-track directions, respectively. e_{R}, e_{S}, e_{W}, for example, denote the unit direction vectors in the three directions. U is the argument of latitude. In addition to X_{K} and X_{P}, the stochastic velocity pulses, denoted as X_{Sto}, are estimated to compensate for other mis-modeled accelerations. X_{Sto} components, presented into the RSW-directions, are spaced with pre-defined intervals T_{Sto}. The A_{K}, A_{P} and A_{Sto} in Eq. (1) represent the partial derivatives of the LEO satellite orbits with respect to the Keplerian elements at the initial condition, the dynamic parameters X_{P} and the stochastic velocity pulses X_{Sto}, respectively. A_{K} and A_{P} are numerically integrated to the epoch t_i based on the variational equations (Beutler 2005), and A_{Sto} is formed as a linear combination of A_{K} (Dach et al. 2015).

With the a priori dynamic models (Table 1) and the estimated orbital parameters, denoted as $\widehat{X}_{\mathrm{K}}$, $\widehat{X}_{\mathrm{P}}$ and $\widehat{X}_{\mathrm{Sto}}$, the LEO satellite orbits are numerically integrated based on the equation of the satellite motion, not only to epochs within the fitting interval T_{fit}, but also to epochs within a pre-defined prediction interval T_{Pre}. The extended orbits are denoted as $\widehat{X}_{\mathrm{Pre}}$. The orbital prediction errors refer here to the differences between the predicted orbits $\widehat{X}_{\mathrm{Pre}}$ and the estimated orbits $\widehat{X}_{\mathrm{L}}$ at the same epoch within the prediction interval T_{Pre}.

The projection of the orbital errors on the signal direction eventually influences the positioning of the users. To evaluate the orbital prediction errors, the root mean square (RMS) of the orbital user range errors (OURE) is used for the assessment. It corresponds to the RMS of the projected orbital errors on the signal direction in a global average sense, which can be expressed as (Reid et al. 2018):

$$\sigma_{\mathrm{OURE}} = \sqrt{\omega_{\mathrm{R}}^2\sigma_{\mathrm{R}}^2 + \omega_{\mathrm{S,W}}^2(\sigma_{\mathrm{S}}^2 + \sigma_{\mathrm{W}}^2)} \tag{6}$$

Table 1
Perturbing dynamic terms (acting on LEO satellites) that are a-priori introduced before the parameter fitting based on existing models.

Perturbing dynamic terms	Model
Earth's gravitational attraction	EGM2008 (degree: 120) (Pavlis et al. 2008)
The gravitational attraction of other planets	Planetary ephemeris: DE405 (Standish 1998)
Solid Earth Tides	IERS 2010 (Petit and Luzum 2010)
Ocean Tides	FES2004 (Lyard et al. 2006)

where σ_R, σ_S and σ_W represents the RMS of the radial, along-track and cross-track orbital prediction errors, respectively. The coefficients ω_R and $\omega_{S,W}$ can be calculated based on the orbital height as shown in Chen et al. (2013).

2.2. Orbital user range accuracy

For integrity purposes, the OURE is computed in this section on the worst projection location within the footprint of the LEO satellite. For the GNSS satellites, the worst-location OURE can be calculated as mentioned in Montenbruck et al. (2015) and Wang et al. (2021). In summary, it distinguishes between two cases, namely when the orbital error vector intersects or doesn't intersect with the Earth's sphere. For LEO satellites with much lower orbital altitudes, the Earth is treated in this contribution as an ellipsoid under, e.g., the geodetic reference system 80 (GRS80) with the semi-major axis a of 6378137 m and the flattening factor $1/f = 298.257222101$.

To decide whether the orbital error vector intersects the surface of the Earth's ellipsoid, the following equation system is established where Eq. (7) representing the straight line passing along the orbital error vector $[x_{err}, y_{err}, z_{err}]^T$ (see the green dashed line in Fig. 1), and Eq. (8) denoting the ellipsoid:

$$\frac{x - x_L}{x_{err}} = \frac{y - y_L}{y_{err}} = \frac{z - z_L}{z_{err}} \tag{7}$$

$$\frac{x^2}{a^2} + \frac{y^2}{a^2} + \frac{z^2}{b^2} = 1 \tag{8}$$

where $[x_L, y_L, z_L]^T$ forms the LEO satellite orbital vector, and the Earth's semi-minor axis b is calculated as $a(1-f)$. x, y and z are position variables on the X, Y, Z-axis of the ECEF system.

Introducing Eq. (7) into Eq. (8), we have:

$$\frac{\left(\frac{x_{err}}{z_{err}} z + x_L - \frac{x_{err} z_L}{z_{err}}\right)^2}{a^2} + \frac{\left(\frac{y_{err}}{z_{err}} z + y_L - \frac{y_{err} z_L}{z_{err}}\right)^2}{a^2} + \frac{z^2}{b^2} = 1 \tag{9}$$

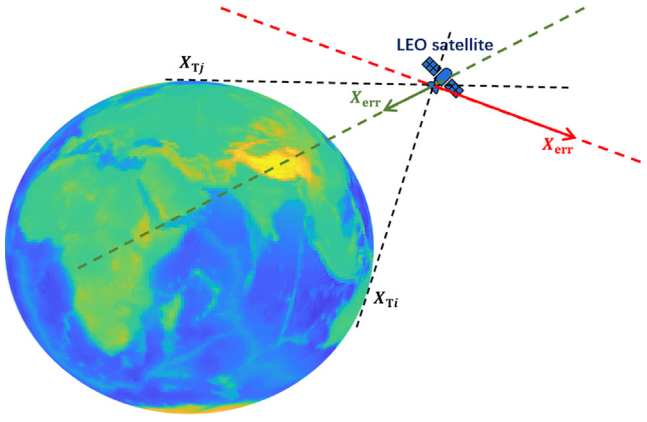

Fig. 1. Relative position between the Earth's ellipsoid, the LEO satellite and the orbital error vector X_{err}.

which can be further simplified as:

$$\beta_2 z^2 + \beta_1 z + \beta_0 = 0 \tag{10}$$

with

$$\beta_2 = \frac{x_{err}^2 + y_{err}^2}{a^2 z_{err}^2} + \frac{1}{b^2} \tag{11}$$

$$\beta_1 = \frac{2}{a^2 z_{err}} \left(x_{err} \left(x_L - \frac{x_{err} z_L}{z_{err}} \right) + y_{err} \left(y_L - \frac{y_{err} z_L}{z_{err}} \right) \right) \tag{12}$$

$$\beta_0 = \frac{(z_{err} x_L - x_{err} z_L)^2 + (z_{err} y_L - y_{err} z_L)^2}{a^2 z_{err}^2} - 1 \tag{13}$$

The orbital error vector intersects the Earth's ellipsoid when Eq. (10) has at least one solution, which implies that the discriminant of the polynomial $\beta_1^2 - 4\beta_2\beta_0 \geq 0$. In such a case, the worst-location OURE, denoted as $OURE_{wl}$, can be calculated as follows:

$$OURE_{wl} = \|X_{err}\|, when \langle X_L, X_{err} \rangle \geq 0 \tag{14}$$

$$OURE_{wl} = -\|X_{err}\|, when \langle X_L, X_{err} \rangle < 0 \tag{15}$$

where $\langle \cdot, \cdot \rangle$ forms the dot product of two vectors. In brief, the absolute value of $OURE_{wl}$ is the norm of the orbital error vector itself, and the sign of $OURE_{wl}$ depends on the direction of the error vector.

In case that Eq. (10) does not have a solution, i.e., when $\beta_1^2 - 4\beta_2\beta_0 < 0$, the orbital error vector (see the red arrow in Fig. 1) does not intersect with the Earth's ellipsoid. In such a case, tangent lines to the Earth's ellipsoid that pass through the LEO satellite are searched (see the black dashed lines in Fig. 1). The one that has the smallest angle with the orbital error vector X_{err} (or $-X_{err}$), is used for the error projection.

The tangent point of any of the tangent lines mentioned above would lay without doubt on the Earth's ellipsoid, with its cartesian coordinates in the ECEF system $X_T = [x_T, y_T, z_T]^T$. Its components are expressed as:

$$x_T = \frac{a}{\sqrt{1 - e^2 \sin^2(\varphi_T)}} \cos(\varphi_T) \cos(\lambda_T) \tag{16}$$

$$y_T = \frac{a}{\sqrt{1 - e^2 \sin^2(\varphi_T)}} \cos(\varphi_T) \sin(\lambda_T) \tag{17}$$

$$z_T = \frac{a(1 - e^2)}{\sqrt{1 - e^2 \sin^2(\varphi_T)}} \sin(\varphi_T) \tag{18}$$

where the Earth's eccentricity e corresponds to $\sqrt{2f - f^2}$. φ_T and λ_T denote the latitude and longitude of the tangent point, respectively. The normal vector of the Earth's ellipsoid passing X_T is expressed as $\left[\frac{2x_T}{a^2}, \frac{2y_T}{a^2}, \frac{2z_T}{b^2}\right]^T$. As the tangent vector is always perpendicular to the normal vector passing X_T on the Earth's Ellipsoid, we have:

$$\left\langle \left[\frac{2x_T}{a^2}, \frac{2y_T}{a^2}, \frac{2z_T}{b^2}\right]^T, [x_T - x_L, y_T - y_L, z_T - z_L]^T \right\rangle = 0 \tag{19}$$

With Eqs. (16)–(18) introduced into Eq. (19), Eq. (19) can be simplified as:

$$b_1\sin(\lambda_T) + b_2\cos(\lambda_T) = b_3, \lambda_T \in (-180^\circ, 180^\circ) \quad (20)$$

with

$$b_1 = y_L \quad (21)$$

$$b_2 = x_L \quad (22)$$

$$b_3 = \frac{a\sqrt{1-e^2\sin^2(\varphi_T)}}{\cos(\varphi_T)} - \tan(\varphi_T)z_L \quad (23)$$

Eq. (20) can further be simplified as:

$$sin\left(\lambda_T + arctan\left(\frac{b_2}{b_1}\right)\right) = \frac{b_3}{\sqrt{b_1^2+b_2^2}}, \lambda_T \in (-180^\circ, 180^\circ) \quad (24)$$

To find the tangent line delivering the smallest angle to X_{err} (or $-X_{err}$), φ_T is search from -90° to 90° with a step of 0.1°. For each φ_{Ti} $(i = 1, \cdots, q)$ with q equal to the number of the searched latitudes, the corresponding λ_{Ti} is solved using Eq. (24). In case that solution(s) exist, the cartesian coordinate vector of the tangent point(s) $X_{Ti} = (x_{Ti}, y_{Ti}, z_{Ti})^T$ can be derived with Eqs. (16)–(18) (see Fig. 1).

As two λ_{Ti} might exist for one φ_{Ti} in Eq. (24), two different tangent points X_{Ti} could exist for one φ_{Ti}. The cosine of the angle θ_i between the vector $(X_L - X_{Ti})$ and the error vector X_{err} is computed as:

$$\cos(\theta_i) = \left\langle \frac{X_L - X_{Ti}}{\|X_L - X_{Ti}\|}, \frac{X_{err}}{\|X_{err}\|} \right\rangle \quad (25)$$

Among all the calculated $\cos(\theta_i)$, the one that delivers the largest $|\cos(\theta_i)|$ is denoted as $\cos(\theta_{max})$. Note that $\cos(\theta_{max})$ could be positive or negative, and it is used for the error projection:

$$\mathrm{OURE}_{wl} = \|X_{err}\| \times \cos(\theta_{max}) \quad (26)$$

In summary, the orbital error vector uses here its largest projection to the Earth's ellipsoid when it doesn't intersect with the Earth's ellipsoid.

Using data over a certain period, with all the OURE_{wl} calculated for a specific LEO satellite over different prediction time periods, the worst-location OURA for a predefined probability of risk p, denoted as $\mathrm{OURA}_{wl,1-p}$, can be expressed for a given prediction interval as:

$$\mathrm{OURA}_{wl,1-p} = \frac{\mathrm{OURE}_{wl,1-p}}{C^{-1}\left(1-\frac{p}{2}\right)} \quad (27)$$

where $\mathrm{OURE}_{wl,1-p}$ represents the value that bounds the absolute value of OURE_{wl} with the probability of $(1-p)$ within a certain prediction interval. $C^{-1}(\cdot)$ represents the inverse of the cumulative distribution function (CDF) of a standard normal distribution at the probability contained in $(\cdot)$. When setting p to 10^{-5}, for example, $C^{-1}\left(1-\frac{10^{-5}}{2}\right)$ is approximately equal to 4.42, and $4.42 \times \mathrm{OURA}_{wl,1-p}$ is assumed to bound all the OURE_{wl} within the prediction interval with a p integrity risk.

3. Results for orbital prediction errors

In this section, the results of the orbital prediction errors are calculated according to the method given in Section 2.1 and next they are analyzed. The appropriate prediction strategies are selected for different satellites and prediction times.

In this study, the prediction strategies differ according to whether the stochastic pulses (X_{sto}) are fitted and used in the prediction or not, and if they are fitted, the length of the selected intervals (T_{Sto}) of the pulses. Note that a short T_{Sto} could be beneficial for reducing the fitting errors, but it is not necessarily good for the prediction. The Keplerian elements at the initial epoch (X_K) and the dynamic parameters (X_P) are always used in the fitting and the prediction. The fitting interval (T_{fit}) differs from 2 h to 24 h, and the prediction is performed up to 6 h with a step of 10 s. The sampling interval of the orbits used for the fitting is 10 s. Table 2 summarizes the details of the studied strategies (A to E), with their applied orbital fitting and prediction parameters. Note that, for strategy B with a time span of 3 h between subsequent stochastic pulses, the X_{Sto} components are not estimated for $T_{fit} < 6$ h. The same applies to the case of $T_{fit} < 4$ h for Strategy C.

For the orbital fitting, high-precision LEO satellite orbits processed by the center for orbit determination in Europe (CODE) are used for the three example LEO satellites used in this study, which have different altitudes. These precise orbits are also used as the reference orbits to evaluate the prediction errors. The three satellites are the GRACE Follow-on satellite GRACE C (Arnold and Jäggi 2020a), the Sentinel-1A satellite (Arnold and Jäggi 2022) and the Sentinel-3B satellite (Arnold and Jäggi 2020b), indicated as GRCC, SE1A and SE3B in the following context, respectively. All three satellites have near-polar orbits. Using the final CODE GPS orbits & clocks and phase biases, the reference orbits were processed in the kinematic mode with enabled ambiguities fixing. Only the orbits flagged by CODE as properly determined, and with a formal standard deviation smaller than 5 cm in each direction, are used for the orbital fitting and the evaluation of prediction errors. As shown in Wang et al. (2020), the orbital border effects are related to the length of the processing interval, which are in a few centimeters even when the processing length is shortened to 12 h. As such, compared to the dm- to sub-meter level prediction errors discussed in this study, the day boundary problem of the reference orbits processed with 24 h intervals is not considered a significant factor that can influence the results. Since

Table 2
Details of the orbital fitting and prediction strategies.

Strategy ID	Fitting interval T_{fit} [h]	Keplerian elements at the initial state	Dynamic parameters	Stochastic pulses	T_{Sto}[h]
A	2,4,6,8,12,24	Yes	Yes	No	–-
B	2,4,6,8,12,24	Yes	Yes	Yes ($T_{\text{fit}}/T_{\text{Sto}}$), when $T_{\text{fit}} \geq 6$h	3
C	2,4,6,8,12,24	Yes	Yes	Yes ($T_{\text{fit}}/T_{\text{Sto}}$), when $T_{\text{fit}} \geq 4$h	2
D	2,4,6,8,12,24	Yes	Yes	Yes ($T_{\text{fit}}/T_{\text{Sto}}$)	1
E	2,4,6,8,12,24	Yes	Yes	Yes ($T_{\text{fit}}/T_{\text{Sto}}$)	0.5

high-precision orbits are used for orbit fitting and prediction, the results could be slightly optimistic.

To evaluate the orbital prediction errors, 365 days in the year 2019–2020 (see Table 3) were used for the fitting. The starting time of each fitting interval was shifted by 1 h in each round of processing, resulting in more than 8000 sets of prediction errors for each prediction strategy and fitting interval, and for each prediction epoch. Days during or shortly before satellite manoeuvres and large data gaps in the reference orbits were not used for the fitting, which results in a longer test interval than the 365 valid test days as shown in Table 3.

As an example, Fig. 2 illustrates the global-averaged σ_{OURE} (Eq. (6)) of the predicted orbits for the GRACE C using the prediction strategies described in Table 2 and fitting intervals from 2 to 24 h. Before calculating the global-averaged OUREs, the radial, along-track and cross-track orbital errors are screened for outliers with the threshold factor $f = C^{-1}\left(1 - \frac{10^{-5}}{2}\right)$ assuming normal distributions of the errors and a significance level 10^{-5}. The data screening is only performed for accuracy purpose in this section, but not for integrity purpose in the next section.

From Fig. 2, it can be seen that the best choice (delivering the smallest σ_{OURE}) of the fitting interval varies when applying different strategies. In general, for predictions of the 503 km-altitude GRACE C of a few hours, a fitting interval of 8–12 h (green and cyan lines) seems to be a good choice for all strategies, although not all strategies deliver good results for a certain prediction time. It can also be noticed that the predictions using a 24 h fitting interval are biased when applying Strategy A (see the red line in the top left panel), as no stochastic pulses are estimated in this strategy (A). In such a case, short variations in the accelerations cannot be captured. This leads to large errors at the edge of the fitting interval and at short prediction periods.

To further illustrate the applicability of different prediction strategies, they are ranked according to their σ_{OURE}, and the strategies with the lowest, second-lowest and the third-lowest σ_{OURE} for prediction times up to 6 h are selected and shown in the left panel of Fig. 3. Despite the frequent changes in the choices among several prediction strategies and fitting intervals, it can be observed that the strategy D with a fitting interval of 12 h (cyan-blue dots) delivers, in general, good σ_{OURE}. The differences among these three σ_{OURE} are not significant.

To avoid frequent changes of strategies and fitting intervals applied for the prediction, the best choice is selected by averaging the σ_{OURE} within each hourly prediction interval. For a given prediction strategy and fitting interval, the averaged σ_{OURE} within interval K, denoted as $\sigma_{\text{OURE},K}$, is calculated as follows:

$$\sigma_{\text{OURE},K} = \sqrt{\frac{\sum_{i=K_1}^{K_n} \sigma^2_{\text{OURE}}(t_i)}{K_n - K_1 + 1}} \tag{31}$$

where K_l denotes the l-th prediction epoch within the interval K ($l = 1, \cdots, n$). n denotes the number of the prediction epochs within K. The strategy and the fitting interval that deliver the lowest $\sigma_{\text{OURE},K}$ within interval K are selected as the best choice for the corresponding interval. The $\sigma_{\text{OURE}}(t_i)$ generated by the best choice are plotted for each interval in the right panel of Fig. 3. As shown by the solid line, the strategy D with a fitting interval of 12 h is the best in an average sense in all the prediction intervals. The prediction errors are dominant in the along-track direction (see the dashed line), which has projected into the signal direction when calculating the OURE according to Eq. (6).

The suitable prediction strategies, fitting intervals and the corresponding σ_{OURE} differ for LEO satellites at different altitudes. The σ_{OURE} generated by the selected prediction strategy and fitting interval within each prediction interval are illustrated for the three test LEO satellites in Fig. 4. The colors are newly selected compared to Fig. 3 for a better illustration and to distinguish between different cases. In general, SE1A and SE3B with higher orbital altitudes have lower σ_{OURE}, with the differences becoming significant for prediction of a few hours. For SE3B, the

Table 3
Details of the LEO reference orbits used for the processing. ω_{R} and $\omega_{\text{S,W}}$ are coefficients used to calculate the OUREs (refer to Eq. (6)).

Satellite	Number of Valid test days	Test period	Average orbital height [km]	Orbital period [h]	ω_{R}	$\omega_{\text{S,W}}$
GRCC	365	January 1, 2019 – January 23, 2020	503 km	1.57	0.457	0.629
SE1A	365	January 6, 2019 – June 21, 2020	704 km	1.65	0.516	0.605
SE3B	365	January 30, 2019 – February 22, 2020	811 km	1.68	0.542	0.594

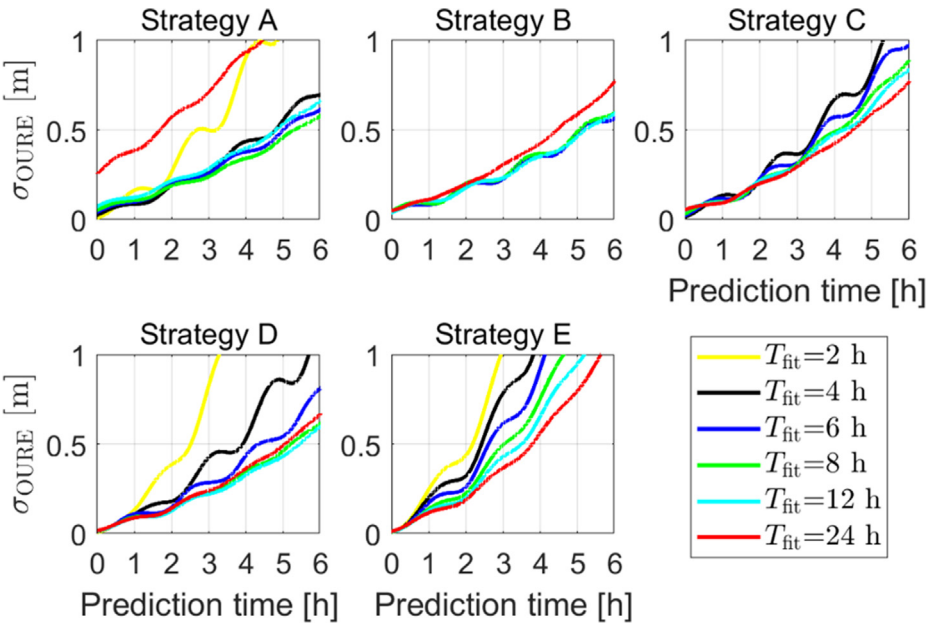

Fig. 2. σ_{OURE} for the predicted orbits of the 503 km altitude GRACE C satellite applying different prediction strategies given in Table 2 and using fitting intervals T_{fit} from 2 h to 24 h (shown in different colours).

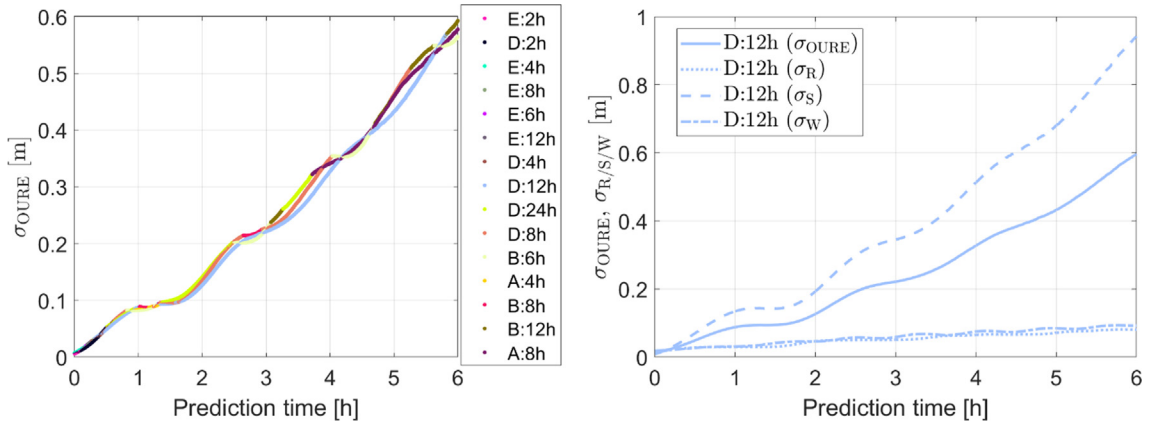

Fig. 3. The lowest, the second-lowest and the third-lowest σ_{OURE} at each prediction epoch (left) and the σ_{OURE} generated by the selected strategy and fitting interval within each hourly prediction interval (right) for GRACE C, which has about 503 km altitude.

prediction strategies A and B are shown to be the better options. For the low-altitude GRACE C, stochastic pulses are suggested to be estimated in shorter intervals of 1 h (Strategy D). From Fig. 4, one can also observe slight periodic behaviors, which correspond to the orbital periods of around 1.5–1.7 h for the three test satellites.

The selected prediction strategies, fitting intervals and the corresponding σ_{OURE} are given for different prediction times and all the three test satellites in Table 4. It can be observed that the orbital altitude is crucial for the achievable σ_{OURE}. At a prediction interval of 4 h, double the value of σ_{OURE} can be observed form GRACE C compared to SE1A and SE3B, and at a prediction interval of 6 h, σ_{OURE} is almost tripled. As the altitudes of SE1A and SE3B are not far away from each other, their σ_{OURE} differences are not significant. For higher LEO satellites of, e.g., around 1000 km, lower σ_{OURE} can be expected when using appropriate prediction strategy, especially for long-term predictions.

4. URA results

This section discusses the OURA at the worst location (see Section 2.2) using real data of the three LEO satellites as in the last section, namely the GRACE C, Sentinel-1A and Sentinel-3B with an altitude of about 503, 704 and

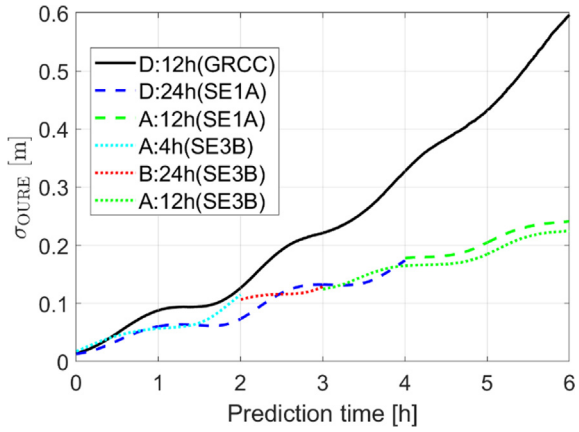

Fig. 4. The σ_{OURE} generated by the selected strategies and fitting intervals within each hourly prediction interval for GRACE C, which has about 503 km altitude (solid line), Sentinel-1A of about 704 km altitude (dashed line) and Sentinel-3B of about 811 km altitude (dotted line).

811 km, respectively. The worst-location OURA are calculated using the worst-location of OUREs ($\mathrm{OURE}_{\mathrm{wl}}$) assuming that the orbital prediction errors are always projected on the worst location on the Earth's ellipsoid. For all the OUREs calculated for a given prediction interval, the value that bound $(1-p)$ of the OUREs is found and denoted as $\mathrm{OURE}_{\mathrm{wl},1-p}$. This value is divided by the factor $C^{-1}\left(1-\frac{p}{2}\right)$ (see Eq. (27)), resulting in the worst-location OURA with the integrity risk p, and is denoted as $\mathrm{OURA}_{\mathrm{wl},1-p}$.

Using the same valid 365 days for orbital fitting and an orbital sampling interval of 10 s as in the last section, the URA is evaluated within each 600 s interval, resulting in more than 500,000 sets of results for each prediction time point. The probability of risk p is assumed 10^{-5}.

The left panel of Fig. 5 shows the $\mathrm{OURA}_{\mathrm{wl},1-p}$ for the 503 km altitude LEO satellite GRACE C. For each bar of 600 s, 99.999 % of the worst-location OURE, $\mathrm{OURE}_{\mathrm{wl},1-p}$, is supposed to be bounded by the blue bars after being multiplied by a factor of about 4.42 (see also the right panel of Fig. 5). For an easier URA adaption, piece-wise overbounding quadratic polynomials are generated to bound all the blue bars at their right boundaries of the 600 s (see the green line). To generate the overbounding polynomials, the best-fit quadratic polynomials of the blue bars, with polynomial coefficients γ_0 (degree 0), γ_1 (degree 1), and γ_2 (degree 2) within each hourly interval, are first produced (see the red line). The overbounding polynomial coefficients $\check{\gamma}_1$ and $\check{\gamma}_2$ are next set to γ_1 and γ_2, respectively, while the overbounding offset $\check{\gamma}_0$ is incremented from γ_0 until the right boundaries of all the blue bars are bounded. The increment step is set to the minimal absolute residual of the polynomial fitting. Within each 600 s prediction interval, the heights of the overbounding bars (see the grey bars) are then set to the overbounding quadratic polynomial (green line) at the corresponding right boundaries. For a certain satellite and a given integrity risk p, when figuring out the prediction interval of the relevant processing time, the user can simply follow the piece-wise overbounding quadratic polynomial with the corresponding coefficients $\check{\gamma}_0$, $\check{\gamma}_1$ and $\check{\gamma}_2$ to compute their $\mathrm{OURA}_{\mathrm{wl},1-p}$. The $\mathrm{OURA}_{\mathrm{wl},1-p}$ shall be usable until the prediction time steps into the next 600 s prediction interval. In this way, $\mathrm{OURA}_{\mathrm{wl},1-p}$ can be computed at any prediction time (within 6 h) just with a few sets of polynomial coefficients.

The $\mathrm{OURA}_{\mathrm{wl},1-p}$ for Sentinel-1A and Sentinel-3B with higher altitudes are smaller than those for GRACE C (see Fig. 6). The grey bars for $\mathrm{OURA}_{\mathrm{wl},1-p}$ within a prediction time of 6 h are lower than 0.5 m. At the prediction time of 1 h, the $\mathrm{OURA}_{\mathrm{wl},1-p}$ are around 0.1 m. The blue bars in both Fig. 5 and Fig. 6 exhibit slight periodic behaviors as shown by the σ_{OURE} in Fig. 4. This is also the reason that hourly quadratic polynomials are utilized to overbound the $\mathrm{OURA}_{\mathrm{wl},1-p}$, which leads to relatively small differences between the overbounding $\mathrm{OURA}_{\mathrm{wl},1-p}$ (grey bars) and real $\mathrm{OURA}_{\mathrm{wl},1-p}$ (blue bars). The overbounding piecewise polynomial coefficients are given in Table 5 for all the three test satellites.

With a longer polynomial fitting interval, fewer polynomial coefficients need to be provided to the users, but resulting in a worse fitting of the real $\mathrm{OURA}_{\mathrm{wl},1-10^{-5}}$. As an example, Fig. 7 shows the overbounding $\mathrm{OURA}_{\mathrm{wl},1-10^{-5}}$ for Sentinel-1A when extending the polynomial fitting interval from 1 h to 2 h and 6 h. In general, fewer polynomial coefficients lead to larger overbounding $\mathrm{OURA}_{\mathrm{wl},1-10^{-5}}$. In Table 6, the overbounding $\mathrm{OURA}_{\mathrm{wl},1-10^{-5}}$ are given for the three test satellites, for different prediction time periods,

Table 4
The selected prediction strategy, fitting interval (in parenthesis) and prediction OURE at different prediction times.

Prediction time [h]	Prediction strategy			σ_{OURE}[m]		
	GRCC (503 km)	SE1A (704 km)	SE3B (811 km)	GRCC	SE1A	SE3B
0.5	Strategy D (12 h)	Strategy D (24 h)	Strategy A (4 h)	0.05	0.04	0.04
1				0.09	0.06	0.06
2				0.13	0.07	0.12
3			Strategy B (24 h)	0.22	0.13	0.13
4			Strategy A (12 h)	0.33	0.17	0.16
5		Strategy A (12 h)		0.43	0.20	0.18
6				0.60	0.24	0.22

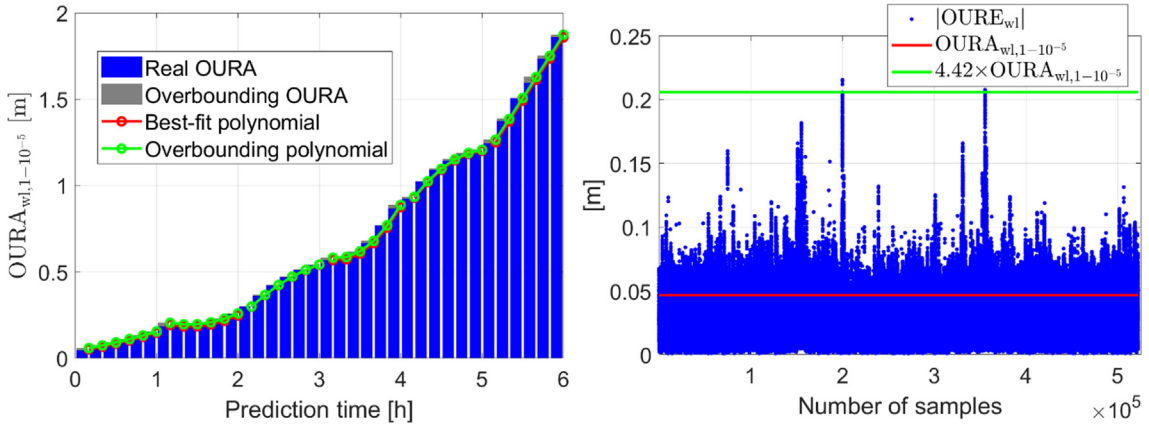

Fig. 5. (Left) The worst-location OURA with an integrity risk of 10^{-5} ($OURA_{wl,1-10^{-5}}$) for 600 s prediction intervals, and (right) the $|OURE_{wl}|$, $OURA_{wl,1-10^{-5}}$ and $4.42 \times OURA_{wl,1-10^{-5}}$ for the first 600 s prediction interval. The data of GRACE C (503 km altitude) were used for the plots.

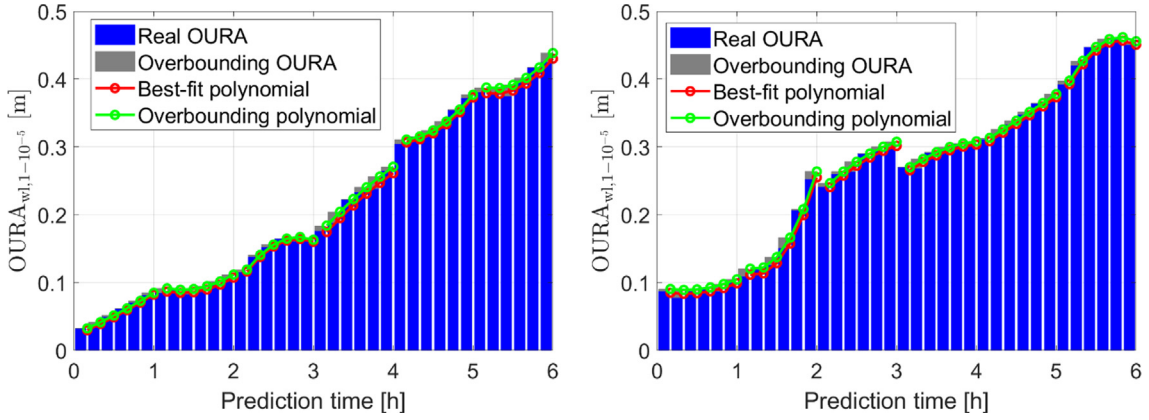

Fig. 6. The worst-location OURA with an integrity risk of 10^{-5} ($OURA_{wl,1-10^{-5}}$) for 600 s prediction intervals. The $OURA_{wl,1-10^{-5}}$ are generated for Sentinel-1A (704 km altitude) and Sentinel-3B (811 km altitude).

Table 5
Coefficients of the overbounding piece-wise polynomial coefficients for the three test satellites (GRACE C, Sentinel-1A, Sentinel-3B) using a fitting interval of 1 h.

Prediction interval [h]	Overbounding piece-wise polynomial coefficients								
	GRACE C			Sentinel-1A			Sentinel-3B		
	γ_0[m]	γ_1[m/h]	γ_2[m/h^2]	γ_0[m]	γ_1[m/h]	γ_2[m/h^2]	γ_0[m]	γ_1[m/h]	γ_2[m/h^2]
0–1	0.04	0.08	0.03	0.02	0.05	0.01	0.09	-0.03	0.04
1–2	0.55	-0.50	0.18	0.19	-0.15	0.05	0.48	-0.59	0.24
2–3	-1.41	1.15	-0.17	-0.75	0.65	-0.12	-0.20	0.30	-0.04
3–4	5.91	-3.31	0.51	-0.49	0.30	-0.03	-0.39	0.34	-0.04
4–5	-7.24	3.32	-0.33	1.60	-0.63	0.08	0.06	0.05	0.00
5–6	-2.24	0.63	0.01	3.12	-1.04	0.10	-4.89	1.85	-0.16

and for different polynomial fitting intervals. When using a polynomial fitting interval of 1 h, for the two Sentinel satellites of about 700–800 km, the $OURA_{wl,1-10^{-5}}$ is around 0.1 m at a prediction time of 1 h, and at sub-meter at a prediction time of 6 h.

5. Discussions

In addition to the LEO satellite orbital altitudes, other factors such as the satellite volume, mass and geometric structure may also influence accelerations caused by, e.g.,

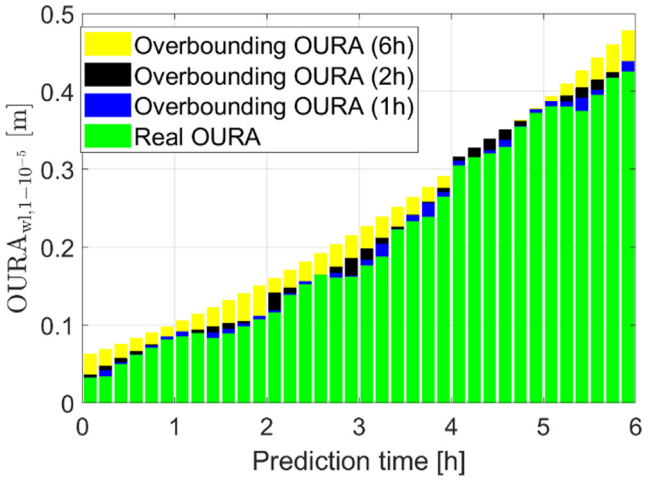

Fig. 7. The computed $OURA_{wl,1-10^{-5}}$ and the overbounding $OURA_{wl,1-10^{-5}}$ for Sentinel-1A with a polynomial fitting interval of 1, 2 and 6 h.

solar radiation pressure and air drag. Table 7 gives the sizes, volumes and masses of the three test satellites used in this study (NASA 2018; ESA 2022a,b). In this study, the three test satellites are used to demonstrate the proposed approaches, namely, the selection of the best prediction strategy based on the OURE, and the estimation of the ellipsoidal OURA and their polynomials for the overbounding OURA. The obtained results could be considered applicable to satellites of similar sizes and masses, but are not intended to be rigid values for all LEO satellites at the altitudes of the three test satellites. For a specific LEO satellite, it is suggested to repeat the selection procedure using the methodology proposed in this contribution to optimize the prediction parameters. The demonstration results obtained in this study do not attempt to serve as references for LEO satellites with significantly different sizes/masses, e.g., the space stations.

6. Conclusions

High-accuracy orbit prediction is essential for real-time single-receiver positioning. For GNSS satellites, the orbits can be predicted for hours with a rather high accuracy. For LEO satellites, which have much lower altitudes and complicated force perturbations, the accuracy and integrity of the orbital prediction need to be assessed for different prediction time periods and satellites of different altitudes.

In this contribution, the orbital prediction errors are assessed using real data from three LEO satellites, i.e., the GRACE C satellite, Sentinel-1A and Sentinel-3B, with altitudes of 503, 704, and 811 km, respectively. Considering the six Keplerian elements at the initial state and the constant, sine and cosine terms of the once-*per*-revolution dynamic parameters, different prediction strategies were tested for stochastic velocity pulses defined for different suggested interval time lengths. The fitting interval of the orbital parameters varies from 2 h to 24 h. It was found that the high-altitude satellites, especially for long-term prediction, favour a strategy that does not consider frequent estimation of the stochastic pulses, while for the GRACE C, which has a lower altitude, it is suggested to use hourly stochastic pulses. For both Sentinel satellites, the global-averaged OURE is at the sub-dm level at a prediction time of 1 h, and around 0.2 m at a prediction time of 6 h.

In addition to the prediction accuracy, the OURA is of interest for integrity purposes. The worst-location OURE is first calculated based on an algorithm proposed for the Earth's ellipsoid. With an assumed integrity risk of 10^{-5},

Table 6
The overbounding $OURA_{wl,1-10^{-5}}$ of the three test satellites at different prediction time periods. The values are given for a polynomial fitting interval of 1, 2 and 6 h.

Prediction time [h]	Overbounding $OURA_{wl,1-p}$ [m]								
	GRACE C			Sentinel-1A			Sentinel-3B		
	1 h	2 h	6 h	1 h	2 h	6 h	1 h	2 h	6 h
0.5	0.09	0.11	0.17	0.05	0.06	0.08	0.09	0.10	0.14
1	0.15	0.17	0.21	0.08	0.08	0.10	0.10	0.11	0.18
2	0.26	0.26	0.35	0.11	0.11	0.15	0.26	0.25	0.25
3	0.54	0.57	0.59	0.16	0.19	0.21	0.31	0.30	0.32
4	0.89	0.87	0.92	0.27	0.28	0.29	0.31	0.31	0.39
5	1.21	1.27	1.34	0.38	0.37	0.38	0.38	0.41	0.44
6	1.87	1.90	1.86	0.44	0.43	0.48	0.46	0.49	0.50

Table 7
Sizes, volumes and masses of the three test satellites.

Satellite	Size	Volume (m^3)	Mass (kg)
GRCC	1.943 m × 3.123 m × 0.78 m	4.73	600
SE1A	2.8 m × 2.5 m × 4 m	28	2300
SE3B	2.2 m × 2.2 m × 3.7 m	17.91	1150

the OURA is computed for 600 s prediction intervals. To ease the user adaption of the proposed methods, piecewise quadratic polynomials are proposed, which are designed to overbound all the 600 s OURA with predefined prediction intervals, so that only a few sets of polynomial coefficients are needed to compute the overbounding OURA at any prediction time. Based on real data assessment, using hourly polynomial fitting for the high-altitude Sentinel satellites, the overbounding OURA is at around 0.1 m at the prediction time of 1 h, and at the sub-meter level at a prediction time of 6 h.

Declaration of Competing Interest

The authors declare that they have no known competing financial interests or personal relationships that could have appeared to influence the work reported in this paper.

Acknowledgements

This research is funded by the National Time Service Center, Chinese Academy of Sciences (CAS) (No. E167SC14), the National Natural Science Foundation of China (No. 12073034), and the Australian Research Council, discovery project No. DP 190102444. We acknowledge also the support of the international GNSS monitoring and assessment system (iGMAS) at the National Time Service Center, and the National Space Science Data Center, National Science & Technology Infrastructure of China (http://www.nssdc.ac.cn).

References

Allahvirdi-Zadeh, A., Wang, K., El-Mowafy, A., 2021. POD of small LEO satellites based on precise real-time MADOCA and SBAS-aided PPP corrections. GPS Solutions 25, 31. https://doi.org/10.1007/s10291-020-01078-8.

Arbinger, C., D'Amico, S., 2004. Impact of Orbit Prediction Accuracy on Low Earth Remote Sensing Flight Dynamics Operations. In: Proceedings of the 18th International Symposium on Space Flight Dynamics (ESA SP-548). Jointly organised by the German Space Operations Center of DLR and the European Space Operations Centre of ESA. 11–15 October 2004, Munich, Germany, pp. 73–78.

Arnold, D., Jäggi, A., 2020a. AIUB GRACE-FO kinematic orbits, release 01. Published by Astronomical Institute, University of Bern. https://doi.org/10.7892/boris.147231. Accessed on March 22, 2022 at http://www.aiub.unibe.ch/download/LEO_ORBITS/GRACE-FO.

Arnold, D., Jäggi, A., 2020b. AIUB Sentinel-3B kinematic orbits, release 01. Published by Astronomical Institute, University of Bern. https://doi.org/10.7892/boris.147287. Accessed on March 22, 2022 at http://www.aiub.unibe.ch/download/LEO_ORBITS/Sentinel-3B.

Arnold, D., Jäggi, A., 2022. AIUB Sentinel-1A kinematic orbits, release 02. Published by Astronomical Institute, University of Bern. https://doi.org/10.48350/165606. Accessed on March 22, 2022 at http://www.aiub.unibe.ch/download/LEO_ORBITS/Sentinel-1A.

Beutler, G., 2005. Variational equations. In: Methods of Celestial Mechanics; Astronomy and Astrophysics Library; Springer: Berlin, Heidelberg, Germany, pp. 175–207.

Cakaj, S., Kamo, B., Lala, A., Rakipi, A., 2014. The Coverage Analysis for Low Earth Orbiting Satellites at Low Elevation. Int. J. Adv. Comput. Sci. Appl. 5, 6. https://doi.org/10.14569/IJACSA.2014.050602.

Chen, L., Jiao, W., Huang, X., Geng, C., Ai, L., Lu, L., Hu, Z., 2013. Study on signal-in-space errors calculation method and statistical characterization of BeiDou navigation satellite system. In: Sun, J., Jiao, W., Wu, H., Shi, C. (Eds.), Proceedings of the China Satellite Navigation Conference (CSNC) 2013. Lecture Notes in Electrical Engineering, vol. 243, Springer, Berlin, Heidelberg, Germany.

Dach, R., Lutz, S., Walser, P., Fridez, P., 2015. Bernese GNSS Software Version 5.2. University of Bern, Bern Open Publishing, Bern, Switzerland. https://d.org/10.7892/boris.72297.

ESA, 2022a. Facts and Figures, Sentinel-1. Accessed on 30 June 2022 at https://www.esa.int/Applications/Observing_the_Earth/Copernicus/Sentinel-1/Facts_and_figures.

ESA, 2022b. Facts and Figures, Sentinel-3. Accessed on 30 June 2022 at https://www.esa.int/Applications/Observing_the_Earth/Copernicus/Sentinel-3/Facts_and_figures.

Ge, H., Li, B., Ge, M., Zang, N., Nie, L., Shen, Y., Schuh, H., 2018. Initial assessment of precise point positioning with LEO enhanced global navigation satellite systems (LeGNSS). Remote Sens. 10 (7), 984. https://doi.org/10.3390/rs10070984.

Ge, H., Li, B., Ge, M., Nie, L., Schuh, H., 2020. Improving low Earth orbit (LEO) prediction with accelerometer data. Remote Sens. 12 (10), 1599. https://doi.org/10.3390/rs12101599.

Gu, D., Ju, B., Liu, J., Tu, J., 2017. Enhanced GPS-based GRACE baseline determination by using a new strategy for ambiguity resolution and relative phase center variation corrections. Acta Astronaut. 138, 176–184. https://doi.org/10.1016/j.actaastro.2017.05.022.

Hadas, T., Bosy, J., 2015. IGS RTS precise orbits and clocks verification and quality degradation over time. GPS Solutions 19, 93–105. https://doi.org/10.1007/s10291-014-0369-5.

Hauschild, A., Tegedor, J., Montenbruck, O., Visser, H., Markgraf, M., 2016. Precise onboard orbit determination for LEO satellites with real-time orbit and clock corrections. In: Proc. ION GNSS+ 2016, Institute of Navigation, Portland, Oregon, USA, September 12–16, pp. 3715–3723.

He, C., Yang, Y., Carter, B., Zhang, K., Hu, A., Li, W., Deleflie, F., Norman, R., Wu, S., 2020. Impact of thermospheric mass density on the orbit prediction of LEO satellites e2019SW002336. Space Weather 18. https://doi.org/10.1029/2019SW002336.

Jia, X., Lv, T., He, F., Huang, H., 2017. Collaborative Data Downloading by Using Inter-Satellite Links in LEO Satellite Networks. IEEE Trans. Wireless Commun. 16 (3), 1523–1532. https://doi.org/10.1109/TWC.2017.2647805.

Johnston, G., Riddell, A., Hausler, G., 2017. The International GNSS Service. In: Teunissen, P.J.G., Montenbruck, O. (Eds.), Springer Handbook of Global Navigation Satellite Systems. Springer Handbooks. Springer, Cham, Switzerland, pp. 967–982. https://doi.org/10.1007/978-3-319-42928-1_33.

Li, X., Ma, F., Li, X., Lv, H., Bian, L., Jiang, Z., Zhang, X., 2018a. LEO constellation-augmented multi-GNSS for rapid PPP convergence. J. Geod. 93, 749–764. https://doi.org/10.1007/s00190-018-1195-2.

Li, K., Zhou, X., Wang, W., Gao, Y., Zhao, G., Tao, E., 2018b. Xu K (2018b) Centimeter-Level Orbit Determination for TG02 Spacelab Using Onboard GNSS Data. Sensors 18 (8), 2671.

Lyard, F., Lefevre, F., Letellier, T., 2006. Francis O (2006) Modelling the global ocean tides: Modern insights from FES2004. Ocean Dyn. 56, 394–415.

Mao, X., Arnold, D., Girardin, V., Villiger, A., Jäggi, A., 2021. Dynamic GPS-based LEO orbit determination with 1 cm precision using the Bernese GNSS Software. Adv. Space Res. 67 (2), 788–805. https://doi.org/10.1016/j.asr.2020.10.012.

Michalak, G., Glaser, S., Neumayer, K.H., 2021. König R (2021) Precise orbit and Earth parameter determination supported by LEO satellites, inter-satellite links and synchronized clocks of a future GNSS. Adv. Space Res. 12 (68), 4753–4782. https://doi.org/10.1016/j.asr.2021.03.008.

Montenbruck, O., Steigenberger, P., Hauschild, A., 2015. Broadcast versus precise ephemerides: a multi-GNSS perspective. GPS Solutions 19, 321–333. https://doi.org/10.1007/s10291-014-0390-8.

NASA, 2018. GRACE-FO Launch Press Kit. National Aeronautics and Space Administration, May 2018. Accessed on 30 June 2022 at https://www.jpl.nasa.gov/news/press_kits/grace-fo/download/grace-fo_launch_press_kit.pdf.

NAVSTAR, 2021. NAVSTAR GPS Space Segment/Navigation User Interfaces. IS-GPS-200, Revision M, 21 May 2021.

Pavlis, N.K., Holmes, S.A., Kenyon, S.C., Factor, J.K., 2008. An Earth gravitational model to degree 2160: EGM2008. EGU 2008, Vienna, Austria, 13–18 April 2008.

Petit, G., Luzum, B., 2010. IERS Conventions. IERS Technical Note, 36. Frankfurt am Main: Verlag des Bundesamts für Kartographie und Geodäsie, 179 pp., ISBN: 3-89888-989-6.

Reid, T.G.R., Neish, A.M., Walter, T., Enge, P.K., 2018. Broadband LEO Constellations for Navigation. J. Inst. Navig. 65 (2), 205–220.

RTS Contributors, 2022. RTS Contributors + Providers, Real-Time Analysis Centers. Accessed on February 21, 2022 at https://igs.org/rts/contributors/#real-time-analysis-centers.

Springer, T.A., Hugentobler, U., 2001. IGS ultra rapid products for (near-) real-time applications. Phys. Chem. Earth Part A. 26 (6–8), 623–628. https://doi.org/10.1016/S1464-1895(01)00111-9.

Standish, E.M., 1998. JPL Planetary and Lunar Ephemerides, DE405/LE405. JPL IOM 312, F-98-048, 1998.

Wang, K., El-Mowafy, A., 2020. Proposed orbital products for positioning using mega-constellation LEO satellites. Sensors 20 (20), 5806. https://doi.org/10.3390/s20205806.

Wang, K., Allahvirdi-Zadeh, A., El-Mowafy, A., Gross, J.N., 2020. A Sensitivity Study of POD Using Dual-Frequency GPS for CubeSats Data Limitation and Resources. Remote Sens. 12 (13), 2107. https://doi.org/10.3390/rs12132107.

Wang, K., El-Mowafy, A., Rizos, C., 2021. Integrity monitoring for precise orbit determination of LEO satellites. GPS Solutions 26 (1), 32. https://doi.org/10.1007/s10291-021-01200-4.

Wang, K., El-Mowafy, A., Wang, W., Yang, L., Yang, X., 2022. Integrity Monitoring of PPP-RTK Positioning. Part II: LEO Augmentation. Remote Sens. 14 (7), 1599. https://doi.org/10.3390/rs14071599.

Wang, Y., Zhong, S., Wang, H., Ou, J., 2016. Precision Analysis of LEO Satellite Orbit Prediction. Acta Geodaetica et Cartographica Sinica 45 (9), 1035–1041. https://doi.org/10.11947/j.AGCS.2016.20160045.

Wermuth, M., Hauschild, A., Montenbruck, O., Kahle, R., 2012. TerraSAR-X precise orbit determination with real-time GPS ephemerides. Adv. Space Res. 50, 549–559. https://doi.org/10.1016/j.asr.2012.03.014.

Yang, L., 2019. The Centispace-1: A LEO Satellite-Based Augmentation System. In: The 14th Meeting of the International Committee on Global Navigation Satellite Systems. Bengaluru, India, 8–13 December 2019.